Military Technical College
Kobry Elkobbah,
Cairo, Egypt
May 27-29,2008

4th International Conference on
Mathematics and Engineering
Physics (ICMEP-4)

AN EULERIAN VLASOV CODE FOR THE NUMERICAL SIMULATION OF WAKE-FIELD ACCELERATION

M. Shoucri

Institut de recherche d'Hydro-Québec (IREQ), Varennes, Québec, Canada, J3X 1S1

ABSTRACT
We use an Eulerian Vlasov code for the numerical solution of the fully relativistic one-dimensional (1D) Vlasov-Maxwell equations, to study the generation of plasma wake fields by intense laser pulses. The very low noise level of the Vlasov code allows to study accurately the physics of the particles acceleration by the wake-field, in the very low density of the phase-space.

1. INTRODUCTION

Large amplitude wake fields can be produced by propagating ultrahigh power, short laser pulses in plasmas. When the laser power is high enough, the electron oscillation (quiver) velocity becomes relativistic, and large amplitude wake fields are generated which support acceleration gradients much greater than those obtained in conventional linear accelerators. In the laser wake-field accelerator concept, a correctly placed trailing electron bunch can be accelerated by the longitudinal electric field and focused by the transverse electric field of the wake plasma waves. Some important aspects of this problem and other nonlinear problems related to large amplitude laser-plasma interactions have been discussed using fluid quantities assumed to satisfy the cold relativistic fluid equations (see for instance [1,2], see also the recent review article in [3]).

In the present work, we study the problem of the laser wake-field acceleration by using an Eulerian Vlasov code for the numerical solution of the 1D relativistic Vlasov-Maxwell equations. A fully nonlinear 1D relativistic Vlasov-Maxwell model to study the self-consistent interaction of intense laser pulses with plasmas can be found, for instance, in [4,5]. A characteristic parameter of a high power laser beam is the normalized vector potential $\left|\vec{a}_\perp\right| = \left|e\vec{A}_\perp / M_e c^2\right| = a_0$, where $\vec{A}_\perp$ is the vector potential, e and M_e are the electronic charge and mass respectively, and c the speed of light. We are interested in the regime $a_0 \geq 1$. The code we use applies a numerical scheme based on a two-dimensional advection technique, of second order accuracy in time-step, where the value of the distribution function is advanced in time by interpolating in two dimensions along the characteristics using a tensor product of cubic *B*-splines [6,7]. Eulerian Vlasov codes have been successfully applied in recent years to study several problems in plasma physics, especially problems associated with wave-particle interaction (see the recent review article in [8]). Interest in Eulerian grid-based Vlasov solvers arise from the very low noise level associated with these codes, which allows accurate representation of the low density regions of the phase-space. Other numerical methods like particle in cell (PIC) codes can lead to phase-space

errors and unphysical numerical heating in the simulation. It was indeed reported in [9] that the results obtained by the PIC codes show a momentum spread inside the laser pulse which is excessively and unphysically large, and hence kinetic effects in the phase-space structure will be poorly approximated in the simulation. This is obviously an important deficiency, especially if the physics of interest is in the low density region of phase-space or in the high energy tail of the distribution function, as is the case in the present problem, since at high laser intensities this can lead to spurious trapping of erroneously large levels. However, since the early work in [10,11] which applied the second-order fractional step scheme for the solution of the Vlasov-Poisson system, the direct solution of the Vlasov equation as a partial differential equation in phase-space, which is used in the present work, has become an important method for the numerical solution of the Vlasov equation, especially due to its numerical stability and its very low noise level [8,12,13].

2. THE RELEVANT EQUATIONS

2.1 *The 1D relativistic Vlasov-Maxwell model*

The general form of the Vlasov equation is written for the present problem in a 4D phase-space for the electron distribution function $F_e(x, p_{xe}, p_{ye}, p_{ze}, t)$ and the ion distribution function $F_i(x, p_{xi}, p_{yi}, p_{zi}, t)$ (one spatial dimension) as follows :

$$\frac{\partial F_{e,i}}{\partial t} + m_{e,i}\frac{p_{xe,i}}{\gamma_{e,i}}\frac{\partial F_{e,i}}{\partial x} \mp \mu\left(\vec{E} + \frac{\vec{p} \times \vec{B}}{\gamma_{e,i}}\right)\cdot\frac{\partial F_{e,i}}{\partial \vec{p}_{e,i}} = 0 \qquad (1)$$

with $\gamma_{e,i} = \left(1 + m_{e,i}^2(p_{xe,i}^2 + p_{ye,i}^2 + p_{ze,i}^2)\right)^{1/2}$ (2)

The upper sign in Eq.(1) is for electrons and the lower sign for ions, and subscripts *e* or *i* denote electrons or ions respectively. Time *t* is normalized to the inverse electron plasma frequency ω_{pe}^{-1}, length is normalized to $l_0 = c\omega_{pe}^{-1}$, velocity and momentum are normalized respectively to the velocity of light *c* and to $M_e c$. In our normalized units $m_e = 1$ and $m_i = \frac{M_e}{M_i}$.

We write the Hamiltonian of a particle in the electromagnetic field of the wave:

$$H_{e,i} = \frac{1}{m_{e,i}}(\gamma_{e,i} - 1) \mp \mu\varphi . \qquad (3)$$

where φ is the scalar potential. Eq.(1) can be reduced to a two-dimensional phase-space Vlasov equation as follows. The canonical momentum $\vec{P}_{ce,i}$ connected to the particle momentum $\vec{p}_{e,i}$ by the relation $\vec{P}_{ce,i} = \vec{p}_{e,i} \mp \mu\vec{a}$. $\vec{a} = e\vec{A}/M_e c$ is the normalized vector potential. From Eq.(3), we can write:

$$H_{e,i} = \frac{1}{m_{e,i}}\left(\left(1 + m_{e,i}^2(\vec{P}_{ce,i} \pm \vec{a})^2\right)^{1/2} - 1\right) \mp \mu\varphi . \qquad (4)$$

Choosing the Coulomb gauge ($div\vec{a} = 0$) , we have for our one dimensional problem $\frac{\partial a_x}{\partial x} = 0$, hence $a_x = 0$. The vector potential $\vec{a} = \vec{a}_\perp(x,t)$, and we also have the following relation along the longitudinal direction:

$$\frac{dP_{cxe,i}}{dt} = -\frac{\partial H_{e,i}}{\partial x} \tag{5}$$

And since there is no transverse dependence :

$$\frac{d\vec{P}_{c\perp e,i}}{dt} = -\nabla_{\perp} H_{e,i} = 0 . \tag{6}$$

This last equation means $\vec{P}_{c\perp e,i} = \text{const}$. We can choose this constant to be zero without loss of generality, which means that initially all particles at a given *(x,t)* have the same perpendicular momentum $\vec{p}_{e,i} = \pm \vec{a}_{\perp}(x,t)$. The Hamiltonian now is written:

$$H_{e,i} = \frac{1}{m_{e,i}} \left(\left(1 + m_{e,i}^2 p_{xe,i}^2 + m_{e,i}^2 a_{\perp}^2(x,t)\right)^{1/2} - 1 \right) \mu \varphi(x,t) . \tag{7}$$

The 4D distribution function $F_{e,i}(x, p_{xe,i}, \vec{p}_{\perp e,i}, t)$ can now be reduced to a 2D distribution function $f_{e,i}(x, p_{xe,i}, t)$:

$$F_{e,i}(x, p_{xe,i}, \vec{p}_{\perp e,i}, t) = f_{e,i}(x, p_{xe,i}, t)\delta(\vec{p}_{\perp e,i} \mu \vec{a}_{\perp}) . \tag{8}$$

$f_{e,i}(x, p_{xe,i}, t)$ verify the relation:

$$\frac{df_{e,i}}{dt} = \frac{\partial f_{e,i}}{\partial t} + \frac{\partial H_{e,i}}{\partial p_{xe,i}} \frac{\partial f_{e,i}}{\partial x} - \frac{\partial H_{e,i}}{\partial x} \frac{\partial f_{e,i}}{\partial p_{xe,i}} = 0 . \tag{9}$$

Which gives the following Vlasov equations for the electrons and the ions::

$$\frac{\partial f_{e,i}}{\partial t} + m_{e,i} \frac{p_{xe,i}}{\gamma_{e,i}} \frac{\partial f_{e,i}}{\partial x} + (\mu E_x - \frac{m_{e,i}}{2\gamma_{e,i}} \frac{\partial a_{\perp}^2}{\partial x}) \frac{\partial f_{e,i}}{\partial p_{xe,i}} = 0 . \tag{10}$$

where $\gamma_{e,i} = \left(1 + \left(m_{e,i} p_{xe,i}\right)^2 + \left(m_{e,i} a_{\perp}\right)^2\right)^{1/2}$.

$$E_x = -\frac{\partial \varphi}{\partial x} \qquad \text{and} \qquad \vec{E}_{\perp} = -\frac{\partial \vec{a}_{\perp}}{\partial t} \tag{11}$$

and Poisson's equation is given by:

$$\frac{\partial^2 \varphi}{\partial x^2} = \int f_e(x, p_{xe}) dp_{xe} - \int f_i(x, p_{xi}) dp_{xi} \tag{12}$$

The transverse electromagnetic fields E_y, B_z and E_z, B_y for the circularly polarized wave obey Maxwell's equations. With $E^{\pm} = E_y \pm B_z$ and $F^{\pm} = E_z \pm B_y$, we have:

$$(\frac{\partial}{\partial t} \pm \frac{\partial}{\partial x}) E^{\pm} = -J_y . \; ; \qquad (\frac{\partial}{\partial t} \mu \frac{\partial}{\partial x}) F^{\pm} = -J_z \tag{13}$$

Which are integrated along their vacuum characteristic *x=t*. In our normalized units we have the following expressions for the normal current densities:

$$\vec{J}_{\perp} = \vec{J}_{\perp e} + \vec{J}_{\perp i} \;; \qquad \vec{J}_{\perp e,i} = -\vec{a}_{\perp} m_{e,i} \int_{-\infty}^{+\infty} \frac{f_{e,i}}{\gamma_{e,i}} dp_{xe,i} \,. \tag{14}$$

2.2 *The numerical scheme*

The numerical scheme to advance Eq.(10) from time t_n to t_{n+1} necessitates the knowledge of the electromagnetic field $E^{\pm}$ and $F^{\pm}$ at time $t_{n+1/2}$. This is done using a centered scheme where we integrate Eq.(13) exactly along the vacuum characteristics with $\Delta x = \Delta t$, to calculate $E^{\pm n+1/2}$ and $F^{\pm n+1/2}$ as follows:

$$E^{\pm}(x \pm \Delta t, t_{n+1/2}) = E^{\pm}(x, t_{n-1/2}) - \Delta t J_y(x \pm \Delta t/2, t_n) \tag{15}$$

$$\text{with } J_y(x \pm \Delta t/2, t_n) = \frac{J_y(x \pm \Delta x, t_n) + J_y(x, t_n)}{2}$$

A similar equation can be written for $F^{\pm n+1/2}$. From Eq.(11) we also have $\vec{a}_{\perp}^{\,n+1} = \vec{a}_{\perp}^{\,n} - \Delta t \vec{E}_{\perp}^{\,n+1/2}$, from which we calculate $\vec{a}_{\perp}^{\,n+1/2} = (\vec{a}_{\perp}^{\,n+1} + \vec{a}_{\perp}^{\,n})/2$. To calculate $E_x^{n+1/2}$, two methods have been used. A first method calculates E_x^n from $f_{e,i}^{\,n}$ using Poisson's equation, then we use a Taylor expansion::

$$\begin{aligned} & E_x^{n+1/2} = E_x^n + \frac{\Delta t}{2}\left(\frac{\partial E_x}{\partial t}\right)^n + 0.5\left(\frac{\Delta t}{2}\right)^2 \left(\frac{\partial^2 E_x}{\partial t^2}\right)^n ; \\ & \text{with } \left(\frac{\partial E_x}{\partial t}\right)^n = -J_x^n ; \qquad \left(\frac{\partial^2 E_x}{\partial t^2}\right)^n = -\left(\frac{\partial J_x}{\partial t}\right)^n \end{aligned} \,. \tag{16}$$

and $J_x^n = m_i \int_{-\infty}^{+\infty} \frac{p_{xi}}{\gamma_i} f_i^{\,n} dp_{xi} - m_e \int_{-\infty}^{+\infty} \frac{p_{xe}}{\gamma_e} f_e^{\,n} dp_{xe}$

A second method to calculate $E_x^{n+1/2}$ is to use Ampère's equation: $\frac{\partial E_x}{\partial t} = -J_x$, from which $E_x^{n+1/2} = E_x^{n-1/2} - \Delta t J_x^n$. Both methods gave the same results. (We have used this second method in the results presented in section 3). Now given $f_{e,i}^{\,n}$ at mesh points (we stress here that the subscript *i* denotes the ion distribution function), we calculate the new value $f_{e,i}^{\,n+1}$ at mesh points from the relation (see [6-8] for details):

$$f_{e,i}^{\,n+1}(x, p_{xe,i}) = f_{e,i}^{\,n}(x - 2\Delta_{xe,i}, p_{xe,i} - 2\Delta_{p_{xe,i}}) \;; \quad . \tag{17}$$

$\Delta_{xe,i}$ and $\Delta_{p_{xe,i}}$ are calculated from the solution of the characteristics equations for Eq.(10), which are given by:

$$\begin{aligned} & \frac{dx}{dt} = m_{e,i} \frac{p_{xe,i}}{\gamma_{e,i}} \\ & \frac{dp_{xe,i}}{dt} = \mu E_x - \frac{m_{e,i}}{2\gamma_{e,i}} \frac{\partial a_{\perp}^2}{\partial x} \end{aligned} \,. \tag{18}$$

This calculation is effected as follows. We rewrite Eq.(17) in the vectorial form:

$$f_{e,i}^{\,n+1}(\mathbf{X}_{e,i}) = f_{e,i}^{\,n}(\mathbf{X}_{e,i} - 2\Delta_{\mathbf{X}e,i}) \;; \quad . \tag{19}$$

$\mathbf{X}_{e,i}$ is the two dimensional vector $\mathbf{X}_{e,i} = \left(x, p_{xe,i}\right)$, and $\Delta_{\mathbf{X}e,i} = (\Delta_{xe,i}, \Delta_{p_{xe,i}})$ is the two dimensional vector calculated from the implicit relation:

$$\Delta_{\mathbf{X}e,i} = \frac{\Delta t}{2}\mathbf{V}_{e,i}(\mathbf{X}_{e,i} - \Delta_{\mathbf{X}e,i}, t_{n+1/2}) \ . \tag{20}$$

$\mathbf{V}_{e,i} = \left(m_{e,i}\frac{p_{xe,i}}{\gamma_{e,i}}, \mu E_x^{n+1/2} - \frac{m_{e,i}}{2\gamma_{e,i}}\frac{\partial (a_\perp^{(n+1/2)})^2}{\partial x} \right)$. Eq.(20) for $\Delta_{\mathbf{X}e,i}$ is implicit and is solved iteratively: $\Delta^{k+1}_{\mathbf{X}e,i} = \frac{\Delta t}{2}\mathbf{V}_{e,i}(\mathbf{X}_{e,i} - \Delta^{k}_{\mathbf{X}e,i}, t_{n+1/2})$, where we start the iteration with $\Delta_{\mathbf{X}e,i}$=0 for k=0. Usually two or three iterations are sufficient to get a good convergence. Then $f_{e,i}^{n+1}$ is calculated from $f_{e,i}^{n}$ in Eq.(17) by calculating the shifted value using two-dimensional interpolation in the two dimensional phase-space $(x, p_{xe,i})$. Similarly in Eq.(20) the shifted value was calculated at every iteration using a two-dimensional interpolation. These two-dimensional interpolations are effected using a tensor product of cubic *B*-splines. The interpolation function is written in the form (see for details [6-8]):

$$s(x, p_x) = \sum_{j=0}^{N_r}\sum_{k=0}^{N_\theta} \eta_{jk} B_j(x) B_k(p_x) \tag{21}$$

For the calculation of the coefficients of the *B*-spline interpolation function $s(x, p_x)$, the coefficients η_{jk} are calculated from the values of the function at the grid points. The cubic *B*-spline is defined as follows:

$$B_j(x) = \frac{1}{6h^3}\begin{cases} (x - x_j)^3 & x_j \le x < x_{j+1} \\ h^3 + 3h^2(x - x_{j+1}) + 3h(x - x_{j+1})^2 & \\ \qquad - 3(x - x_{j+1})^3 & x_{j+1} \le x < x_{j+2} \\ h^3 + 3h^2(x_{j+3} - x) + 3h(x_{j+3} - x)^2 & \\ \qquad - 3(x_{j+3} - x)^3 & x_{j+2} \le x < x_{j+3} \\ (x_{j+4} - x)^3 & x_{j+3} \le x < x_{j+4} \end{cases} \tag{22}$$

and $B_j(x) = 0$ otherwise. h is the grid size. A similar definition holds for $B_k(p_x)$.

3. RESULTS

A generous number of grid points has been used in the simulation, to reproduce accurately the fine details which develop in phase-space. N_x =13000 is the number of grid points in space, for a length L = 50.444 . N_{pxe} =1600 is the number of grid points in momentum for the electrons (p_{xmaxe} =20, p_{xmine} = -20). And for the ions N_{pxi} =256 (p_{xmaxi} = 11, p_{xmini} = -11.). We assume the frequency of the laser pulse $\omega_0 / \omega_p >> 1$ ($\omega_0 / \omega_p = 10$ in the

present calculation), and the radiation envelope of the laser pulse changes on a time-scale which is long compared to the wave period. The spatial length of the envelope of the laser pulse is $L = \lambda_p = 2\pi c/\omega_p$, much longer than the laser field wavelength λ. The model is similar to what has been presented in [1,2] for the fluid calculations, with the addition that in the present simulation we include a kinetic 1D relativistic Vlasov equation, and this is done for both electrons and ions. The evolution of the circularly polarized laser pulse is calculated self-consistently with Maxwell's equations. The validity of the 1D model requires that the laser beam transverse dimension $r >> \lambda_p$.

The system is initially neutral ($n_e = n_i$). The density in our normalized units is equal to 1 in the flat central part, with steep gradients and vacuum at both ends. The length of the vacuum region is 0.6 on each side, and the length of the transition region for the density from 0 to the flat value of 1 is 1.4. The electrons and ions have initially a Maxwellian distribution, with a temperature T_e = 3keV for the electrons and T_i = 1keV for the ions. Results with lower temperature have also been obtained, but the results generally show little sensitivity for the temperature (see, for instance, [9,14]). The forward propagating circularly polarized laser pulse is penetrating from the vacuum at the left boundary, and propagate towards the right, and is written in our normalized units as

$E^+ = 2E_0 \sin(\pi\xi/L)\sin(k_0\xi)$ and $F^- = 2E_0 \sin(\pi\xi/L)\cos(k_0\xi)$ for $-L \le \xi \le 0$

(where $\xi = x - t$), and E_0 =0 otherwise. In vacuum we have for the electromagnetic (EM) wave $k_0 = \omega_0 = 10$ (so in our normalized units the wavelength $\lambda = 2\pi/k_0 = 0.628$). We have ten oscillations of the EM wave in the length *L* of the pulse envelope. We choose for the amplitude of the potential vector $a_0 = 1$, so that $E_0 = \omega_0 a_0 = 10$. Since the envelope is slowly varying, we can write for the corresponding vector potential for $t \le 2\pi$: $a_y = -a_0 \sin(\pi\xi/L)\cos(k_0\xi)$, $a_z = a_0 \sin(\pi\xi/L)\sin(k_0\xi)$. At $t = 2\pi$, the entire envelope of length *L* of the forward propagating pulse has penetrated the domain , and is left to evolve self-consistently using Eqs.(13), and $\vec{a}_\perp$ is calculated as indicated in the previous section.

Fig.(1) shows the results for the laser pulse at *t*= 21.34 (dash curve), and Fig.(2) shows the results for the laser pulse at *t*= 50.444 after crossing the whole domain and reaching the right boundary. The laser pulse is followed by the wake field E_x (full curve). For the present set of parameters, the pulse has propagated through the plasma with little deformation. Fig.(3) shows at *t*= 21.34 the plot of the electron density (full curve), the ion density (dash curve) and again the axial wake field E_x (dash-dot curve). The pulse has been also added , with its amplitude divided by 10, for reference. The amplitude of E_x reaches since the beginning of the simulation a maximum peak of 0.6 just behind the pulse. This is close to the projected theoretical value for saturation for cold plasma [1,2] given by $E_{x\max} = (\gamma_0^2 - 1)/\gamma_0 = 0.717$, where $\gamma_0 = \sqrt{1 + a_0^2} = \sqrt{2}$. The electron density (initially equal to 1 in the central region) is forming spikes surrounded by depleted regions, and the electric field E_x is rapidly changing sign at these spikes. Fig.(4) shows the equivalent results at *t* = 50.444, when the laser pulse has reached the right boundary. We see again that the peak electric field behind the pulse is still 0.6, and decays slowly as we move away from the pulse. This is in contrast with the results reported for a cold plasma [1,2] in the presence of a circularly polarized wave, which showed the electric field reaching a constant amplitude throughout the domain. This decay of the amplitude of the electric field agrees however with the results reported in [15] for the plasma wake-field accelerators, in the presence of a circularly polarized wave (in

the plasma wakefield accelerators, an electron bunch is used, instead of the laser pulse, to excite the wake field). Note the electric field E_x shows a steeper variation at the right of Fig.(4) compared to the profile at the left, and the period of E_x is slightly longer for the oscillation at the right of Fig.(4), compared to the period of oscillation of E_x at the left of Fig.(4). The density peak at the right in Fig.(4) (full curve) is reaching a value of 2.2, which is the same value of the equivalent peak in Fig.(3). So the front peaks seem to be following the laser pulse with little deformation. Note that the first thin peak density at the left in Fig.(3) results from the interaction of the pulse with the region of the sheath along the edge gradient. This peak varies rapidly and remained very localized in the sheath region at the edge, and did not interfere with the stable pattern which appears on the flat top of the density profile. Figs(5-8) show the phase-space for the electron distribution function at t =21.34, 38.88, 42.68 and 50.444. Note there is a population which seems to detach itself from the bulk and follows the modulation of the bulk, and then accelerates when it reaches the position of a peak of the electric field. Fig.(9) shows the ion distribution function at t=50.444. Although the ion density profile (broken curve in Figs(3-4)) appears constant, Fig.(9) shows a modulation in the ion distribution function contour plot. For the relatively short run we have presented, it shows a modulation which has a tendency to increase as we move to the right.

Behind the peak showing the first accelerated beam in Figs(5-8), there is a peak which did not show an accelerated beam, followed by others peaks where accelerated beams are present. We show in Figs.(10-11) the results obtained in another simulation done with the same parameters [16], but with L = 40.35 and different grid sizes N_x = 10000, N_{pxe} =1100 (p_{xmaxe} = 12, p_{xmine} = -12, so the grid size in momentum space was slightly smaller for the results in Fig.(10)). We see in Fig.(10) particles accelerating at every peak behind the first accelerated beam (note the difference in the vertical scale p_{xe}). The reason for this difference is for the moment not very clear and needs further investigation. The peak of the wake electric field behind the laser pulse in Fig.(11) is also also 0.6, and the front density peak is also 2.2. We used the same plotter in both cases (emphasizing slightly the low density regions to make the accelerated beams more visible). We show in Fig.(12) a contour plot emphasizing the region of the tip the front beam in Fig.(7). The lower part in Fig.(12) is a 3D view of the top of the beam and the tail preceding it. It clearly shows at the front edge at the top a well localized beam structure with steep gradient.

3. CONCLUSION

The numerical method used in the present work consists of integrating along the characteristics in the two-dimensional phase-space $\mathbf{X}_{e,i} = \left(x, p_{xe,i}\right)$ the relativistic Vlasov equation , using for interpolation a tensor product of cubic B-spline. Both electrons and ions have been included in the present simulation. The method we are using have shown in previous applications to be accurate, and to give accurate results in the low density regions of the phase-space [6-8]. This is important since numerical results obtained with PIC codes for this problem can lead to unphysical numerical heating in the simulation, and show a momentum spread inside the laser pulse which is unphysically large [9]. Hence the detailed kinetic effects will be poorly approximated in the PIC simulation. The results for the circularly polarized wave we have presented show the peak of the wake field immediately behind the laser pulse is in good agreement with the value calculated using the nonlinear relativistic cold plasma equations [1,2]. The results in Fig.(12) show the code capable of calculating with a very good resolution a very sharp and localized beam structure.

Acknowledgments

The author is grateful to the assistance of Benoit Morin and the Centre de calcul scientifique de l'IREQ (CASIR) for computer time used to do part of this work. The constant support and interest of Dr. André Besner is gratefully acknowledged

References

[1] Sprangle, P., Esarey, E. and Ting, A. 1990 *Phys.Rev*. A41, 4463
[2] Ting, A., Esarey, E. and Sprangle, P. 1990 *Phys.Fluids* B2, 1390
[3] Bingham, R., Mendonca, J.T. and Shukla, P.K. 2004 *Plasma Phys. Control. Fusion* 46 , R1
[4] Akhiezer, A.I. and Polovin, R.V. 1956 *Sov.Phys.JETP* 3, 696
[5] Guérin, S., Laval, G., Mora, P., Adam, J.-C., Héron, A. and Bendib, A. 1995 *Phys.Plasmas* 2, 2807
[6] Shoucri, M., Gerhauser, H. and Finken, K.H. 2003 *Comp.Phys.Comm.* 154, 65
[7] Shoucri, M., Gerhauser, H. and Finken, K.H. 2004 *Comp.Phys.Comm.* 164, 138
[8] Shoucri, M. 2007 ' The method of characteristics for the numerical solution of hyperbolic differential equations', in Computer Physics Research Trends (Ed. Silvan J. Bianco, Nova Science Publishers Inc., NY), Chapter 1.
[9] Shadwick, B.A., Tarkenton, G.M., Esarey, E.,. Schroeder, C.B. 2005 *Phys.Plasmas* 2005 12, 056710-1
[10] Cheng, C.Z. and Knorr, G. 1976 *J.Comp.Phys.* 22, 330
[11] Gagné, R. and Shoucri, M. 1977 J.Comp.Phys. 24, 445
[12] Shoucri, M. 2008 *Nonl.Sci.Num.Simul.* 13, 174
[13] Huot, F., Ghizzo, A., Bertrand, P., Sonnendrücker, E., Coulaud, O. 2003 *J.Comp.Phys.* 185, 512
[14] Shoucri, M. 2008 *Comm.Comp.Phys.* (to be published)
[15]Krall, J., Joyce, G. and Esarey, E. 1991 , Naval Research Lab. Memorandum Report 6772
[16] Shoucri, M. 2007 Proc. of the EPS conference, Warsaw (European Phys. Society, to be Published)

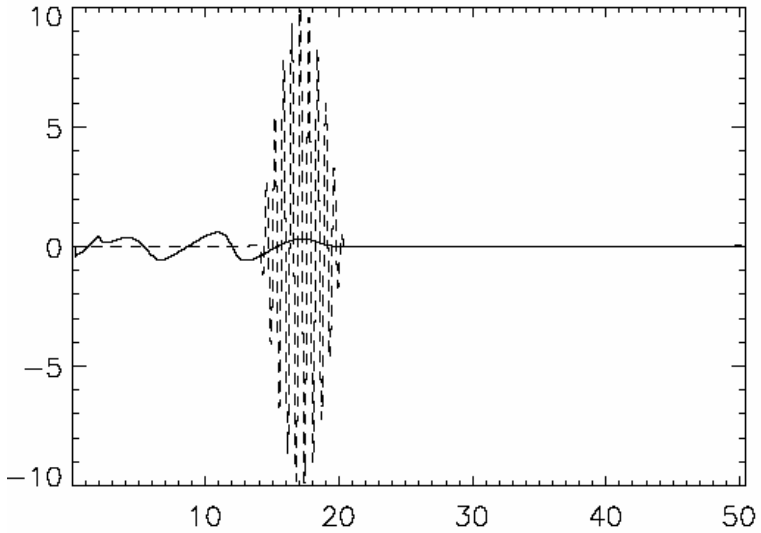

Fig.1: Laser pulse (dash curve) and wake field E_x (full curve) at t=21.34

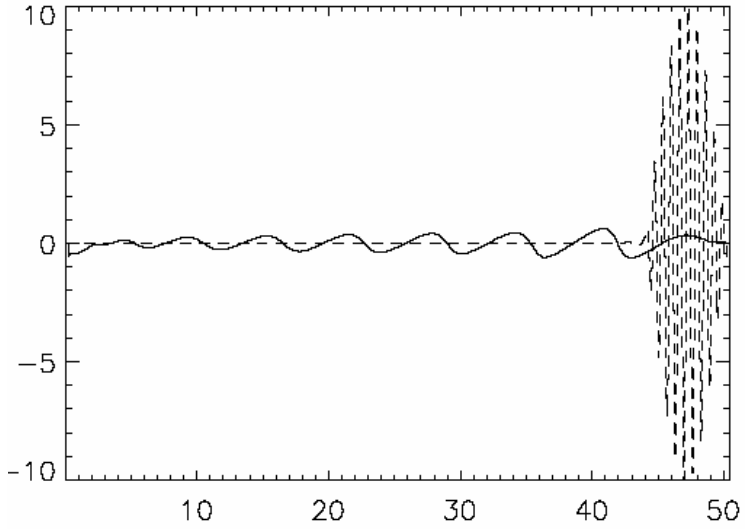

Fig.2: Laser pulse (dash curve) and wake field E_x (full curve) at t=50.444

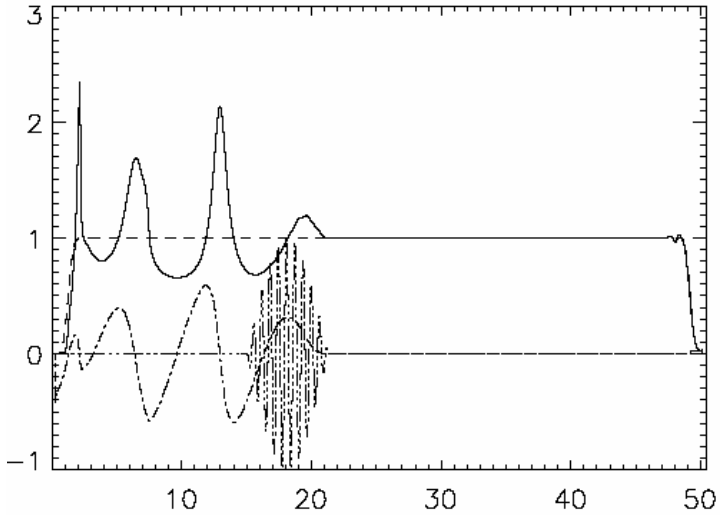

Fig.3: Plot at t = 21.34 of the electron density (full curve), the ion density (dash curve), the axial wake field E_x (dash-dot curve). The laser pulse (amplitude divided by 10) has been also added for reference.

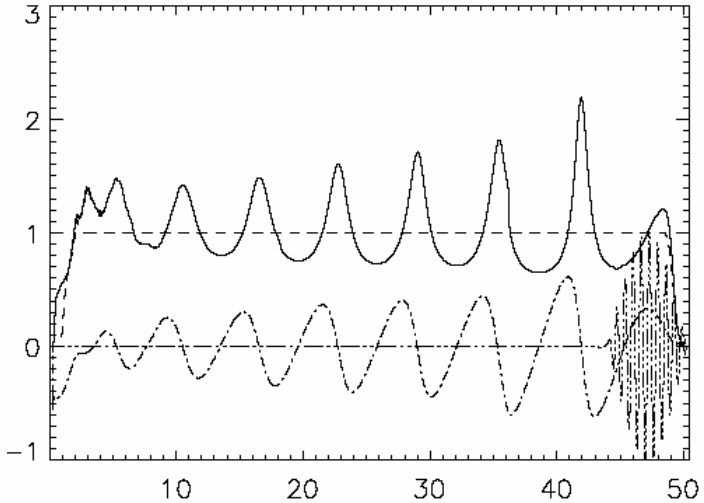

Fig.4 Plot at t = 50.444 of the electron density (full curve), the ion density (dash curve), the axial wake field E_x (dash-dot curve). The laser pulse (amplitude divided by 10) has been also added for reference

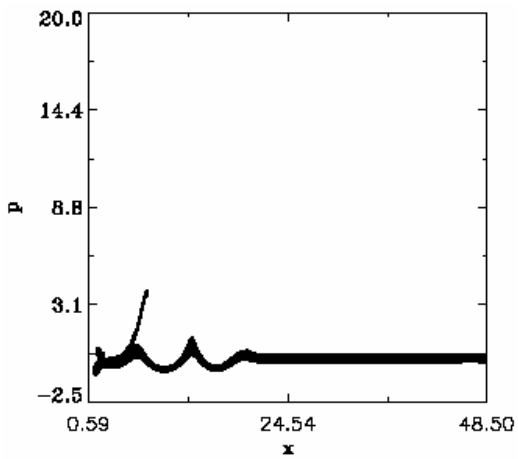

Fig.5 Phase-space contour plot of the electron distribution function at $t = 21.34$

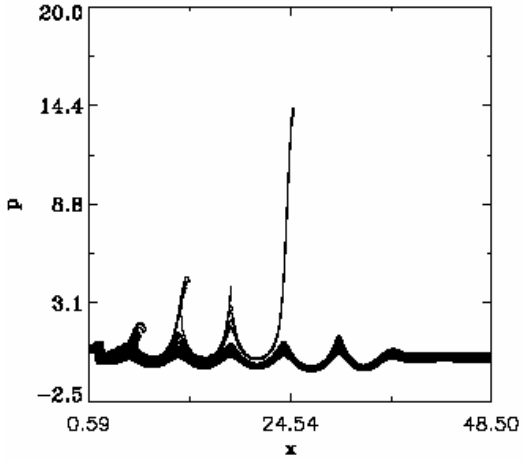

Fig.6 Phase-space contour plot of the the electron distribution function at $t = 42.68$

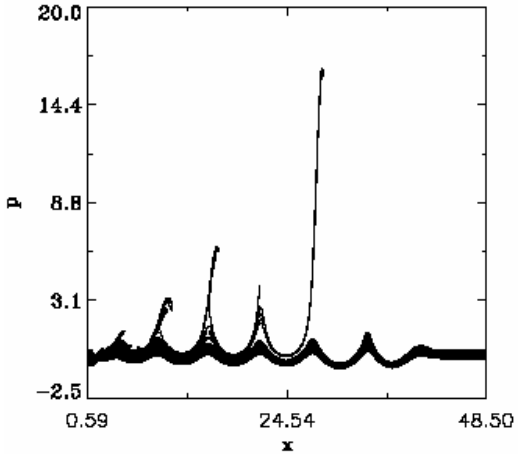

Fig.7 Phase-space contour plot of the electron distribution function at $t = 38.88$

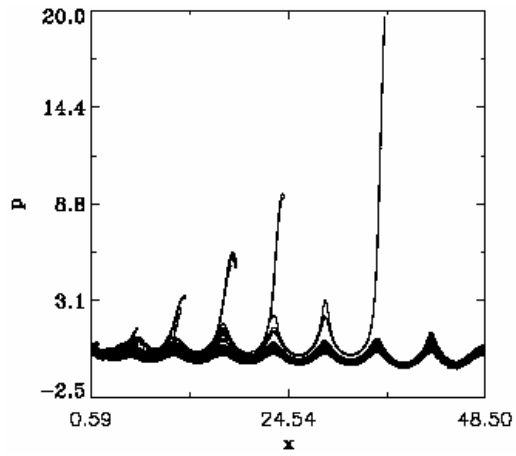

Fig.8 Phase-space contour plot of the electron distribution function at $t = 50.444$

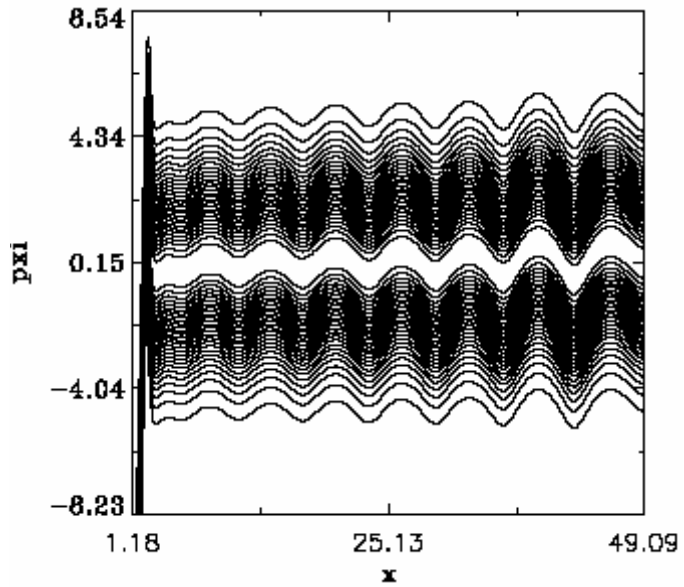

Fig.9 Phase-space contour plot of the ion distribution function at $t = 50.444$

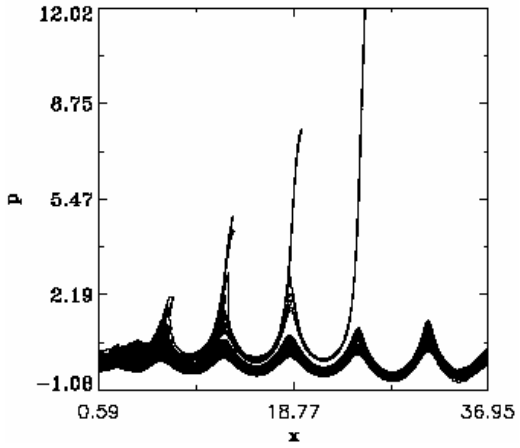

Fig.10 Phase-space contour plot of the electron distribution function at $t = 40.35$ (from the simulation presented in [16]).

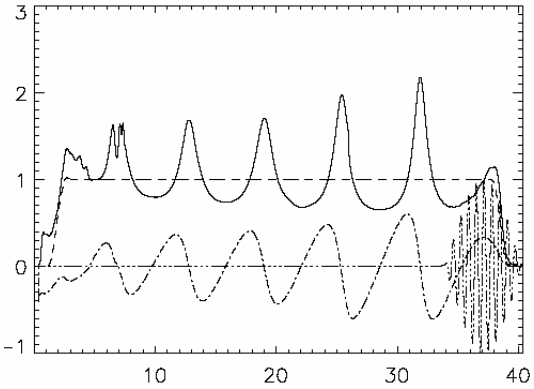

Fig.11 Plot at $t = 40.35$ of the electron density (full curve), the ion density (dash curve), the axial wake field E_x (dash-dot curve). The laser pulse (amplitude divided by 10) has been also added for reference. (from the simulation presented in [16]).

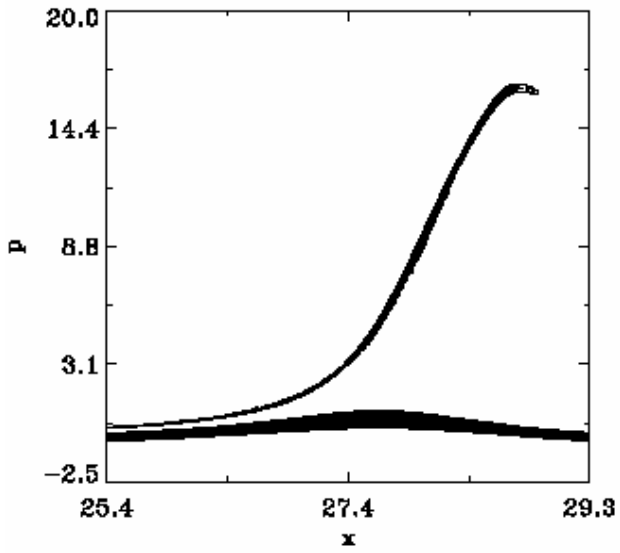

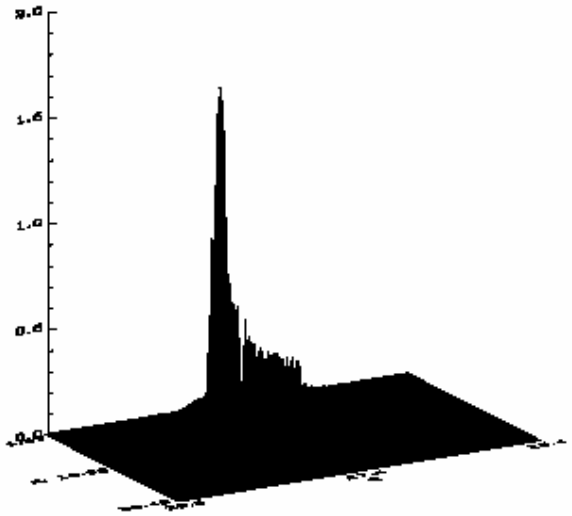

Fig.12 Phase-space contour-plot of the electron distribution function presented in Fig.(6) at t=42.68, concentrating on the region of the front beam. Note the sharp beam structure appearing in the lower 3D plot of the front end of the beam.